Use of streamflow indices to identify the catchment drivers of hydrograph

Jeenu Mathai[1] and Pradeep P. Mujumdar[1,2]

[1]Department of Civil Engineering, Indian Institute of Science, Bangalore, India

[2]Interdisciplinary Centre for Water Research, Indian Institute of Science, Bangalore, India

Correspondence to: Pradeep. P. Mujumdar (pradeep@iisc.ac.in)

Abstract. Time irreversibility or temporal asymmetry refers to the steeper ascending and gradual descending parts of a streamflow hydrograph. The primary goal of this study is to bring out the distinction between streamflow indices directly linked with rising limbs and falling limbs and to explore their utility in uncovering processes associated with the steeper ascending and gradual descending limbs of the hydrograph within the time-irreversibility paradigm. Different streamflow indices are correlated with the rising and falling limbs and the catchment attributes. The key attributes governing rising and falling limbs are then identified. The contribution of the work is on differentiating hydrographs by their time irreversibility features and offering an alternative way to recognize primary drivers of streamflow hydrographs. A series of spatial maps describing the streamflow indices and their regional variability in the Contiguous United States (CONUS) is introduced here. These indices complement the catchment attributes provided earlier (Addor et al., 2017) for the CAMELS data set. Findings of the study revealed that the elevation, fraction of precipitation falling as snow and depth to bedrock mainly characterize the rising limb density, whereas the aridity and frequency of precipitation influence the rising limb scale parameter. Moreover, the rising limb shape parameter is primarily influenced by forest fraction, the fraction of precipitation falling as snow, mean slope, mean elevation, sand fraction, and precipitation frequency. It is noted that falling limb density is mainly governed by climate indices, mean elevation, and the fraction of precipitation falling as snow. However, the recession coefficients are controlled by mean elevation, mean slope, clay, the fraction of precipitation falling as snow, forest fraction, and sand fraction.

1 Introduction

Hydrologists use data to understand the hydrologic system by identifying several unique catchment signatures and employ various flow descriptors independent of statistical assumptions yet capable of capturing signals that reflect the basin's long-term unique behavior. Hydrological indices, commonly referred to as hydrologic metrics, hydrologic signatures, or diagnostic signatures, are quantitative flow metrics that characterize statistical or dynamical hydrological data series (McMillan, 2021). Specifically, streamflow indices are flow descriptors derived from discharge time-series data, and a considerable collection of indices are available to aid in the better characterization of hydrological features, ranging from basic statistics like the mean to more sophisticated metrics (Addor et al., 2018; McMillan, 2021). In many cases, daily streamflow records are not permitted for redistribution; however, researchers have computed streamflow indices and made them publicly accessible.

Hydrological indices are increasingly used in emerging areas such as global-scale hydrologic modeling and large-sample hydrology to extract relevant information and compare the different watershed processes (Addor et al., 2017, 2018; McMillan, 2021). These indices offer an indirect way to explore hydrological processes as well as provide insights into hydrologic behavior in catchments where data other than streamflow is restricted and are widely used in process exploration, model calibration, model selection, and catchment classification (Addor et al., 2018; Clark et al., 2011; Kuentz et al., 2017; McMillan et al., 2011; Sawicz et al., 2011). McMillan (2021) presented a classification that differentiates between statistics and dynamics-based signatures and between signatures at different timescales.

The relevance of time irreversibility (or temporal asymmetry) of streamflow variability on a daily scale has been emphasized in recent studies (Koutsoyiannis, 2020; Mathai and Mujumdar, 2019; Serinaldi and Kilsby, 2016). The disparity in physical mechanisms driving the hydrograph's rising and falling limbs (Fig.1) contributes to time irreversibility. Koutsoyiannis (2020) shows that irreversibility may be ignored at scales relevant to hydrological applications in atmospheric processes, but it is critical to include irreversibility in studies related to streamflow. Streamflow recessions convey valuable information about the basin storage properties and aquifer characteristics (Aksoy & Bayazit, 2000). High variability encountered in the recession behaviour of individual segments is always a challenge in modeling the recession limb (Tallaksen, 1995). Recessions do not follow a simple form due to their nonlinear nature (Aksoy et al., 2001). Various segments of recession represent different stages in the flow process and there is a need to differentiate the recession to various segments and to characterize the recession rates separately. Such segmentation of recession curves enables us to reveal the nonlinear behavior of streamflow dynamics. Time irreversibility must therefore be acknowledged in streamflow analysis, accounting for the distinction of the recession into different segments, with a faster recession induced by high discharges caused by surface runoff and a slower recession caused by baseflow (Fig.1), and the characterization of the recession rates separately (Mathai and Mujumdar, 2019). In this study, streamflow indices are chosen to better understand different hydrological processes by recognizing the streamflow hydrograph's temporal asymmetry. The novelty in the work presented here is to differentiate hydrograph limbs by their time irreversibility property and use their associated indices to provide an approach to derive insights on the primary drivers of streamflow hydrographs.
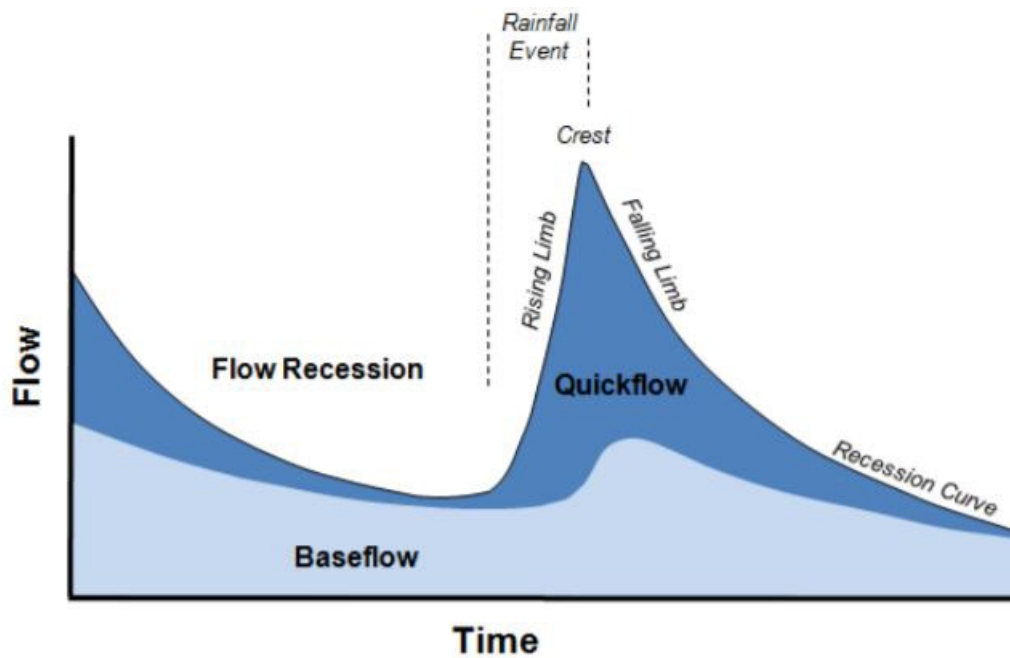
Figure 1. Schematic representation of rising limb and falling limb
(source: Environment Southland;
https://www.es.govt.nz/environment/water/groundwater/groundwater-monitoring)

The analysis employs a collection of indices drawn from hydrograph shape diagnoses, to extract information about the properties of rising and falling limbs of the hydrograph. The principle of time irreversibility is encapsulated by six streamflow indices that characterize the shape of a streamflow hydrograph.

The goals of this study are as follows: i) to identify the key drivers of streamflow hydrograph (rising and falling limbs) in terms of catchment attributes (eg. mean slope, aridity, fraction of precipitation falling as snow) using time-irreversibility-based indices; ii) to present a spatial map-based attribute class based on streamflow indices for a large-sample hydrology dataset. The attribute class is a broad classification of attributes based on a particular aspect/feature. *Topography, climate, and soil* are examples of attribute classes. In this study, we present a new attribute class of streamflow indices related to rising and falling limbs, referred to as *"TI-streamflow indices" (Time-irreversibility streamflow indices)*.

Hydrograph analysis is referred to as the investigation of the numerous factors that influence hydrograph shape (Rogers, 1972). The presence of hydrographs with a similar shape in long-term observation series of runoff suggests that the same conditions of runoff generation reoccur from time to time in the catchment of a river due to climate cyclicity and as a result of hydrological processes (Khrystyuk et al., 2017). Because climatic factors are dynamic in space and time, they seem to be the most significant factors influencing the hydrograph shape provided that changes in catchment conditions like land use are small. Khrystyuk et al., (2017) suggested that for the Desna river basin in Russia, temperature, snow water equivalent, and snowmelt conditions are the most critical factors influencing the shape of hydrographs. However, it is likely that these controls may not be equally important controls on hydrograph across all regions globally. The shape, timing, and peak flow of a streamflow hydrograph are influenced spatially and temporally by rainfall and watershed factors (Singh, 1997). One of the earlier studies by Roberts and Klingeman (1970) investigated the influence of meteorological and physiographic parameters on the runoff hydrograph using a physical laboratory model. Storm-related parameters (rainfall intensity, rainfall duration, storm movement) and basin surface conditions are among the inputs that could be experimentally

89 modified in this model. The results revealed that each of these variables mentioned above has a substantial impact

90 on the hydrograph shape where certain factors had a more considerable effect on the rising limb of the runoff

91 hydrograph, whereas others were more important in terms of the flood crest (Roberts and Klingeman, 1970).

92 As shown in numerous studies in the literature, our notion of time-irreversibility and its indices could also helpful

93 in understanding the catchment drivers of streamflow hydrographs. This study presents an attribute class of

94 hydrograph shape descriptors with temporal asymmetry. The significance of large-sample hydrology datasets in

95 open hydrologic science and their potential to improve hydrological studies' transparency is also underlined in

96 this study.

97 Large-sample hydrology (LSH) gathers information from a large number of catchments to gain a more

98 comprehensive understanding of hydrological processes and to go beyond individual case studies. LSH helps

99 identify catchment behavior and leads one to derive precise conclusions regarding different hydrological

100 processes and models (Addor et al., 2020). Studies involving large-sample catchments help in understanding the

101 drivers of hydrological change (Blöschl et al., 2019), in assessing hydrological similarity and classification

102 (Berghuijs et al., 2014; K. A. Sawicz et al., 2014), in predictions in ungauged basins (Ehret et al., 2014), and in

103 analysing model and data uncertainty (Coxon et al., 2014) and foster hydrology research by standardizing and

104 automating the creation of large-sample hydrology datasets worldwide (Addor et al., 2020). LSH assists in

105 exploring interrelationships between numerous catchment attributes related to landscape, climate, and hydrology

106 (Addor et al., 2017; Alvarez-Garreton et al., 2018; Gupta et al., 2014; Newman et al., 2015; Sawicz et al., 2011)

107 and generalizing rules that can significantly improve the predictability of the water cycle (Alvarez-Garreton et al.,

108 2018).

109 The primary challenges in fostering LSH are data availability and accessibility, which seriously hinder its use in

110 data-scarce regions. Despite the fact that a few large-scale hydrology studies have been undertaken, the number

111 of publicly available large-scale datasets is still restricted (Addor et al., 2017, 2020; Coxon et al., 2020). Moreover,

112 licensing restrictions and strict access policies make the datasets rarely available to the public (Coxon et al., 2020).

113 Model Parameter Estimation Experiment project (MOPEX) dataset (Duan et al., 2006), Canadian model parameter

114 experiment (CANOPEX) database (Arsenault et al., 2016), Global Streamflow Indices and Metadata Archive (Do

115 et al., 2018; Gudmundsson et al., 2018), Global Runoff Reconstruction (Ghiggi et al., 2019), HydroATLAS (Linke

116 et al., 2019) and the Catchment Attributes and MEteorology for Large-Sample studies (CAMELS) (Addor et al.,

117 2017) are notable contributions of open and accessible large-sample catchment datasets (Coxon et al., 2020). The

118 concept of time irreversibility-based streamflow indices is then applied to CAMELS catchments with the goal of

119 encouraging large-sample hydrology studies. The primary contribution of this study is to establish the distinction

120 between signatures directly linked with rising limbs and falling limbs and their utility in uncovering processes

121 associated with the hydrograph's steeper ascending and gradual descending limbs.

122 **2 Methods**

123 To facilitate an understanding of various hydrological processes and streamflow hydrograph drivers, the study

124 employs streamflow indices considering the streamflow hydrograph's temporal asymmetry. The description of

125 indices used in this study are tabulated in Table 1. Streamflow indices linked to each limb of the streamflow

126 hydrograph within the time-irreversibility paradigm are distinguished since hydrographs have rising and falling

limbs. The following indices are considered in the rising limb category: 1) rising limb density, 2) rising limb shape parameter, and 3) rising limb scale parameter. In contrast, 1) falling limb density 2) slope of upper recession (upper recession coefficient) 3) slope of lower recession (lower recession coefficient) are selected in falling limb category. The next step is to compute these indices for a large number of catchments and correlate them with attributes such as climate, topography, vegetation, geology, and soil. The streamflow indices can be correlated explicitly since sub-categories are involved in each of the catchment attributes discussed above. Finally, the key attributes governing rising and falling limbs can be summarized and identified. The specifics of indices are explained further below.

Rising limb density (RLD) is defined as the ratio of the number of rising limbs and the cumulative time of rising limbs (Shamir et al., 2005). RLD is a hydrograph shape descriptor without considering the flow magnitude (Fig. 2) and the expression for RLD is given as,

$$RLD = \frac{N_{RL}}{T_R} \tag{1}$$

The ratio of the number of falling limbs to the cumulative time of falling limbs is termed as falling limb density (FLD) (Fig. 2) (Shamir et al., 2005). The expression for FLD is given as,

$$FLD = \frac{N_{FL}}{T_F} \tag{2}$$

Table 1. Hydrological descriptors with temporal asymmetry.

Attribute		Description	Unit	Data source	References
Rising limb	RLD	Rising limb density	day^{-1}		Shamir et al. (2005)
	a	Rising limb scale parameter	-		Mathai and Mujumdar, (2019)
	b	Rising limb shape parameter	-	N15 – USGS data*	Mathai and Mujumdar, (2019)
Falling limb	FLD	Falling limb density	day^{-1}	(https://doi.org/10.5065/D6MW2F4D)	Shamir et al. (2005)
	b_1	Upper recession coefficient	-		Mathai and Mujumdar, (2019)
	b_2	Lower recession coefficient	-		Mathai and Mujumdar, (2019)

* N15 covers 671 catchments in the contiguous USA (CONUS), which provides daily meteorological forcing and daily streamflow measurements from the United States Geological Survey (USGS).

$$Rising\ limb\ density = \frac{3}{\Delta T1\ +\ \Delta T3\ +\ \Delta T5}$$

$$Falling\ limb\ density = \frac{3}{\Delta T2\ +\ \Delta T4\ +\ \Delta T6}$$
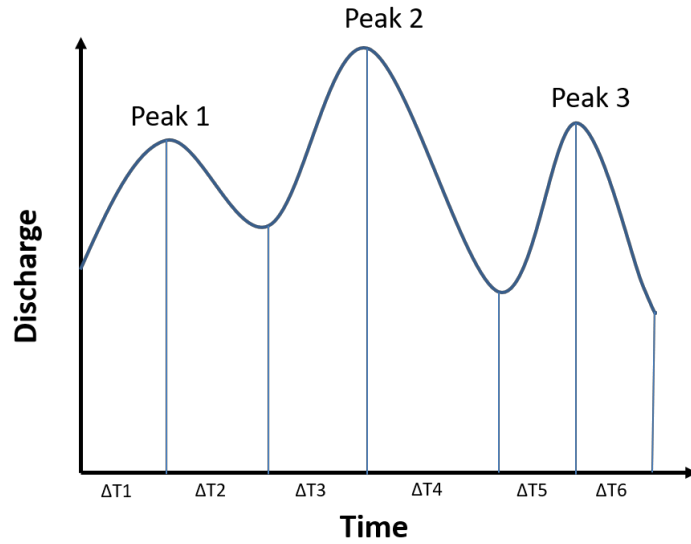
Figure 2. Schematic example of rising limb density (RLD) and falling limb density (FLD) calculation (Shamir et al., 2005).

We first identify the hydrologic state of the stream (ascension and recession) (Mathai and Mujumdar, 2019). To determine the hydrologic state of a stream - increasing (wet) or decreasing (dry) - on a given day, a time series of diurnal increments is extracted by differencing the original time series with its one-day lagged time series. The positive increments are identified as diurnal increments for wet days (ascension limb).
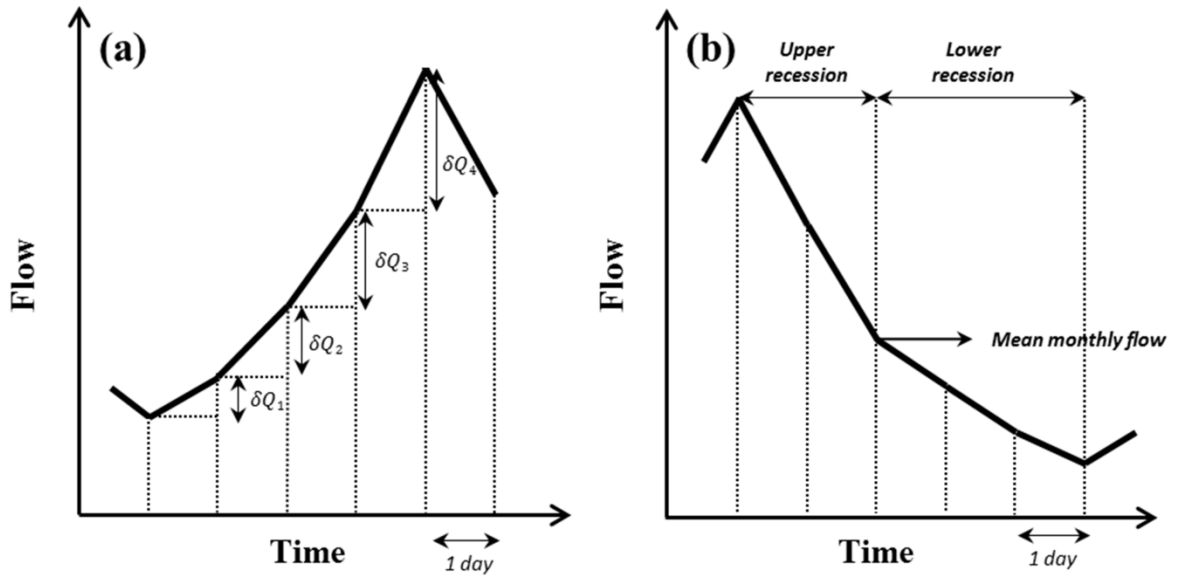
Figure 3. Schematic representation of flow series (a) ascension limb and (b) recession limb (Mathai and Mujumdar, 2019).

155   To characterize the shape of the rising limbs occurring on wet days, the diurnal increments are fitted using an

156   appropriate probability density function. The Weibull distribution reflects the diurnal increments of streamflow

157   that occur on wet days satisfactorily (Mathai and Mujumdar, 2019; Stagge and Moglen, 2013; Szilagyi et al.,

158   2006), and the scale 'a' and shape $'b'$ parameters of the Weibull distribution are computed for each catchment by

159   using observed diurnal increments of streamflow (indicating δQ) of the ascension limb (Fig 3.a). The Weibull pdf

160   is positive only for positive values of x, and is zero otherwise. For strictly positive values of the scale parameter

161   a and shape parameter b, the density function is given by

$$f(x; a, b) = \begin{cases} \dfrac{b}{a}\left(\dfrac{x}{a}\right)^{b-1} e^{-(x/a)^b} & x \geq 0, \\ 0 & x < 0, \end{cases} \tag{3}$$

162   where $a > 0, \; b > 0$. The shape and scale parameters of the Weibull distribution are estimated for each catchment

163   from the observed diurnal increments of the streamflow. The scale parameter controls the magnitude of the rising

164   limb, whilst the shape parameter reflects the flashiness of the rising limb. The scale parameter is related to the

165   magnitude of storm events which mirrors the general shape of flows in the stream. As a result, correlating these

166   parameters with catchment attributes reveals which catchment attributes drive the magnitude and flashiness of

167   rising limbs.

168   In contrast, an exponential recession is used to capture the shape of the falling limbs on dry days of the daily

169   hydrograph, representing the falling limbs' underlying dynamics (Mathai and Mujumdar, 2019). As the upper

170   recession refers to the fast flow following a storm event and the lower recession refers to the baseflow recession,

171   falling limb modeling is done in two stages (Fig 3.b) (Aksoy, 2003; Aksoy and Bayazit, 2000). The steps to obtain

172   recession coefficients b_1 and b_2 are explained below (Mathai and Mujumdar, 2019). To portray the shape of the

173   recession limbs occurring on dry days of the daily hydrograph, an exponential recession is employed to capture

174   the falling limbs' underlying dynamics (Mathai & Mujumdar, 2019). The expression for the exponential recession

175   is given as follows,

$$Q_t = Q_0 e^{-bt} \tag{4}$$

176   where b is the recession coefficient, t is time, Q_t is the flow t days after the peak and Q_0 is the peak flow (Mathai

177   & Mujumdar, 2019). Mean flow value is chosen as an appropriate measure (Sargent, 1979) to divide the recession

178   into two stages. The limbs with a peak flow value greater than the observed mean flow value are considered as

179   upper recessions and those with peak flow values smaller than the observed mean as lower recessions. However,

180   it may be noted that using the mean monthly flow can lead to unusual situations if peak flow for a given event is

181   below the monthly mean. In such cases, the entire recession would be classified as a lower recession curve, and

182   no upper part would exist. In those situations, there are still different driving processes for the first and second

183   part of the recession, but these would all be lumped into one category in this case. Since we are dealing with the

184   long-term time series, the recession slope will be nearly constant for a catchment and does not vary much with

185   the recession separation technique used. In this study, we calculate recession slope at an annual scale. The upper

186   recession is modelled as follows,

$$Q_t = Q_0 e^{-b_1 t} \tag{5}$$

187 where b_1 is the recession coefficient for the upper part of the recession limb, t is the number of days after the

188 peak, Q_t is flow t days after the peak, Q_0 is the preceding peak flow (Mathai & Mujumdar, 2019). The lower

189 recession is represented as,

$$Q_t = Q_0^* e^{-b_2(t-t^*)} \tag{6}$$

190 where b_2 is the recession coefficient for the lower part of the recession limb, t^* is the time from the start of the

191 lower recession, Q_0^* is the initial flow in the lower part of the recession (Mathai & Mujumdar, 2019). The recession

192 expressions for upper and lower recession are fitted by regressing $\ln(Q_t/Q_0)$ versus t and $\ln(Q_t/Q_0^*)$ versus $t -$

193 t^* respectively. These linear regressions are performed on each individual recession sequence. The average of the

194 upper/lower recession parameters is taken as the upper/lower recession parameter of that catchment (on daily time

195 series data).

196 The study uses indices related to rising limb (viz., RLD, rising limb scale parameter, rising limb shape parameter)

197 and recession limb (viz., FLD, upper recession coefficient, lower recession coefficient) to summarize the

198 characteristic shape of steeper rising and gradually declining falling limb and its application in understanding the

199 role of various drivers of catchment attributes in streamflow generation.

3 Dataset used

201 Section 3 provides the description of the dataset used and the study area chosen. This study employs the CAMELS

202 dataset, which encompasses daily discharge data and catchment attributes for 671 catchments (Fig. 4) across the

203 continental United States, representing a diverse set of catchments with long streamflow time series covering a

204 wide range of hydro-climatic conditions (Addor et al., 2017). The time frame chosen for the analysis is from 1

205 October 1989 to 30 September 2009 (Addor et al., 2017).

206 The topographic characteristics of CAMELS dataset are represented in Fig. S1. Except for the Appalachian

207 Mountains, the eastern part of the Continental United States is much flatter than the western portion, according to

208 mean elevation and mean slope maps (Fig. S1.a and S1.b). Figure S1.c depicts the spatial pattern of catchment

209 size, highlighting presence of some catchments with an area greater than 10,000 km². The landscape of each

210 catchment is described using multiple attributes, which can be divided into various classes as shown in Table S1

211 (Addor et al., 2017).

212

213

214
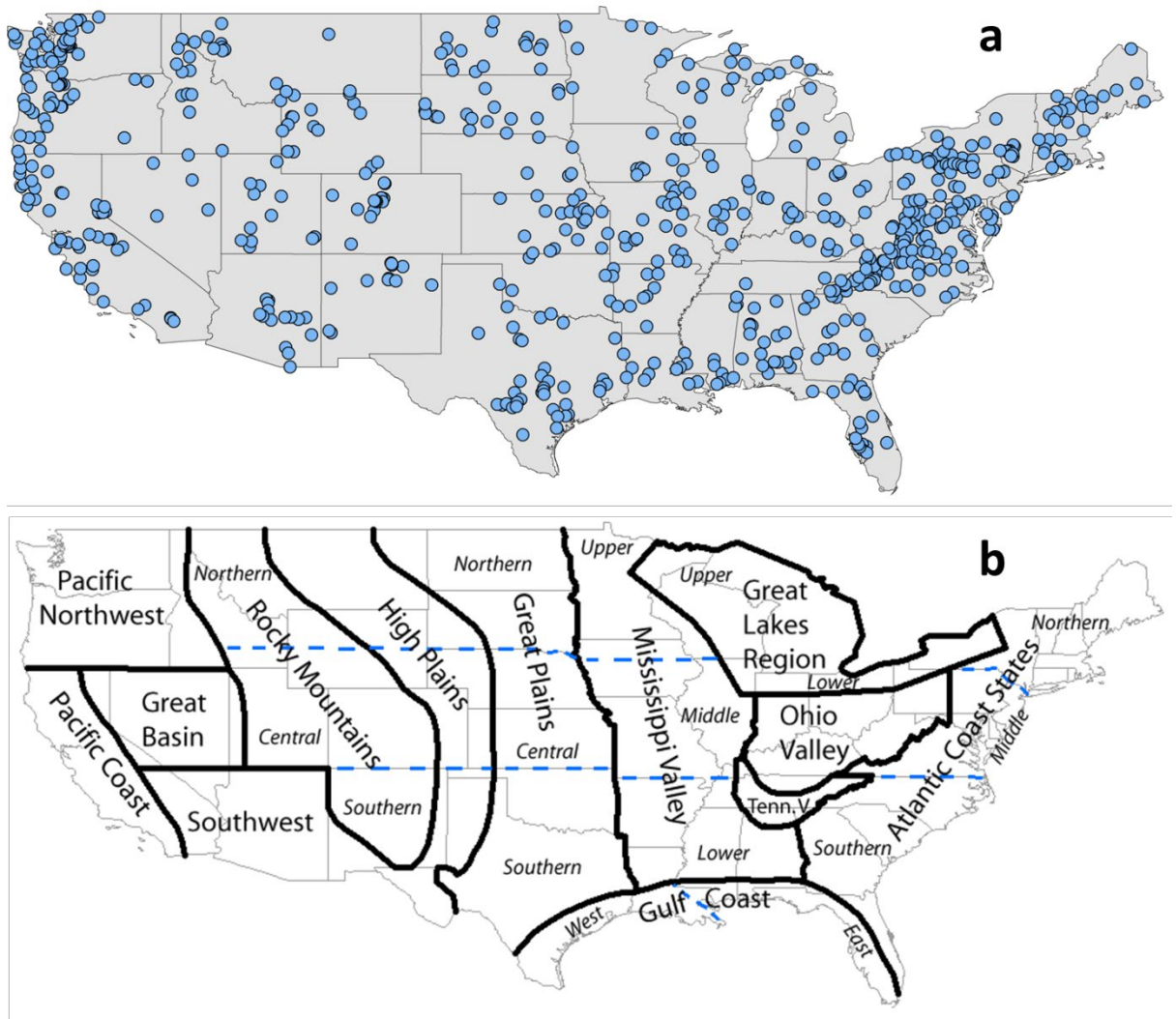
Figure 4. (a) Map of 671 CAMELS catchments in the continental United States considered in this study. (b) Geographical regions of US according to NOAA National Centers for Environmental Information referred for the analysis (source: NOAA National Centers for Environmental Information; https://www.ncdc.noaa.gov/temp-and-precip/drought/nadm/geography).

4 Results and Discussion

The regional variability of the streamflow indices is investigated by computing the rising limb density, falling limb density, rising limb scale parameter, rising limb shape parameter, upper recession coefficient, and lower recession coefficient for 671 CAMELS catchments and given as spatial maps. These spatial maps of streamflow indices complement CAMELS' six main classes of catchment attributes developed (Addor et al., 2017): topography, climate, streamflow, land cover, soil, and geology. The motivation for presenting streamflow indices in the form of spatial maps with respect to geographical regions is to align with spatial maps introduced by the CAMELS dataset. In addition, streamflow indices are also presented in hydrological clusters to incorporate a more explicit spatial representation of catchment behavior across the CONUS. The hydrological clusters are being used to link the current study to the existing catchment classification literature undertaken in the CONUS region.

As catchment attributes cover a broad range of aspects of catchment hydrology such as land cover, soil, climate, geology, topography, and each of the attributes usually does not exist independently in space but is closely interlinked, resulting in various strongly correlated attributes in a catchment (Jehn et al., 2020; Stein et al., 2021), the association between these attributes and streamflow indices is discussed further in the subsequent section. The scope of this work is limited as it does not attempt to explain all interrelations between each attribute; instead, the main objective of the study is to establish the governing catchment attributes of streamflow indices.

Further, previous studies reveal that climate attributes significantly influence catchment streamflow dynamics; hence it is crucial to understand the role of different climatic zones on these six streamflow indices (Addor et al., 2018; Berghuijs et al., 2014; Jehn et al., 2020; Knoben et al., 2018; Stein et al., 2021). Since the chosen 671 catchments are distributed across the US in varied climatic zones (Jehn et al., 2020; Knoben et al., 2018; Stein et al., 2021), the CAMELS dataset is ideal for addressing this question. With this motivation, the effect of climate attributes on streamflow indices associated with rising and falling limbs is also investigated in the last section.

4.1 Spatial Variability in Streamflow Indices and Relation of the Streamflow Indices with Catchment Attributes

Streamflow indices related to rising limbs and falling limbs are computed for the selected catchments and displayed in spatial maps as shown in Fig. 5 and Fig. 7, respectively. The spatial analysis is based on the United States' geographical areas (for details, refer to Fig. 4b) as defined by NOAA's National Centers for Environmental Information and is referred to in the following spatial maps. Furthermore, the clusters provided by Jehn et al. (2020) to represent the discrete hydrological behaviors of the continental United States are adopted in this study to understand the regional variability of catchment behavior. Figure S2 and Table S2 present the location map and details of the ten clusters. Figure S3 shows boxplots of the catchment attributes of the clusters (after Jehn et al., 2020).

Even though a comprehensive dataset such as CAMELS provides an excellent overview of various catchments in contrasting climatic and topographic regions, it does not by itself provide insights to explain hydrologic behavior. We present here streamflow indices in clusters representing distinct hydrological behavior, enabling an understanding of the hydrological processes. Jehn et al. (2020) summarizes the characteristics of each catchment cluster in terms of climate, hydrology and location. The clusters presented by Jehn et al. (2020) are formed based on agglomerative hierarchical clustering with ward linkage on the principal components of the hydrological signatures. The hydrological signatures identified with the highest spatial predictability are used to cluster 643 catchments from the CAMELS dataset (Jehn et al., 2020). This facilitates straightforward interpretations of the observations to explain the hydrologic behavior in each cluster.

In this paper, we first identify the regions in the United States where high/low values of streamflow indices occur. The dominant catchment attributes of these regions are also identified using corresponding clusters. The streamflow indices and the dominant catchment attribute are then related to interpreting the obtained findings. In terms of geographical regions, the rising limb density is highest over the Atlantic coast states, Ohio valley, Lower Mississippi Valley, Southern Great Plains, Southwest and Pacific, and lowest along the Upper Great Lakes region, Upper Mississippi Valley, Great Basin, and Northern Rocky Mountains, Northern Interior Plains, and East of Gulf Coast (Fig. 5.a). Further, in terms of hydrological clusters, the Appalachian Mountains (Cluster 10), Southeastern

and Central Plains (Cluster 1), and all Southern most states of the US (Cluster 9) witness high rising limb densities (Fig. 6.a). Cluster 1 is characterized by high forest fraction and low elevation (Figure S3), resulting in little annual snowfall. Cluster 10 catchments are located in the Appalachian Mountains (Figure S2), with a higher mean elevation than most other clusters, experiencing low aridity and high forest cover (Figure S3). However, Cluster 9 encompasses all of the United States' southern states, with negative precipitation seasonality (winter) and higher forest cover and green vegetation (Figure S3). Furthermore, all of the catchments in Cluster 9 are very near the sea (Figure S2), with a low snow component and high evapotranspiration (Figure S3). We used Spearman rank correlation for the correlation analysis, shown in Table 2. It can be seen that the rising limb density shows a negative correlation (Table 2) with the area (r = -0.30), elevation (r = -0.20) fraction of precipitation falling as snow (r = -0.33), and depth to bedrock (r = -0.32). Northwestern Forested Mountains (Clusters 3, 4), located in the mountains of the western US, experience low values of rising limb density. The catchments of Cluster 3 have a high fraction of precipitation falling as snow (Figure S3). Cluster 4 is found in the western United States' mountains (Figure S2), where there is a lot of snow, same as Cluster 3 (Figure S3). Low values of rising limb density are observed due to a negative correlation with the fraction of precipitation falling as snow (r = -0.33) (Table 2). The study indicates that rising limb density is mainly governed by elevation and fraction of precipitation falling as snow in the CONUS.

Considerably low values of rising limb scale parameters are experienced over the Rocky Mountains, High Plains, Great Plains, Upper Mississippi Valley, Great Basin, Southwest, and the Great Lakes regions, whereas the Pacific Northwest shows high values of rising limb scale parameters (Fig. 5.b). Clusters (5, 7) over the Northwestern Forested Mountains of CONUS (Figure S2) experience very high values of rising limb scale parameters (Fig. 6.b). These catchments have the highest discharge, especially in the early summer, due to a combination of high precipitation and snowmelt (Jehn et al., 2020). Further, the region in the Continental US which receives the highest precipitation is included in Cluster 5 (Jehn et al., 2020). Moreover, Cluster 5 consists of a large proportion of forest (Figure S3). Again, Cluster 7 with high values of rising limb scale parameter (Figure 6.b) is characterized by reasonably high fraction of precipitation falling as snow (Figure S3). High precipitation and snowmelt might result in a large discharge. Higher discharges can create higher values of rising scale parameters as the rising limb scale parameter regulates the magnitude of the rising limb. Low values of rising limb scale parameters are shown by Clusters 2, 8, 9 (Figure 6.b). This is because of low water availability, low snow fraction precipitation falling as snow, and high evaporation experienced in these regions (Jehn et al., 2020). Low discharge and thus lower rising limb scale parameters can be caused by excessive evaporation, low water availability, and a low snow fraction of precipitation falling as snow. It is observed that the rising limb scale parameter (Table 2) shows a negative correlation with climate (r = -0.53 for aridity) and a positive association with the vegetation attributes (r = 0.46 for forest fraction, r = 0.41 for LAI maximum, r = 0.44 for green vegetation fraction maximum). Frequency of precipitation (r = -0.56 for high precipitation frequency, r = -0.63 for low precipitation frequency) display a strong negative association with the rising limb scale parameter (Table 2).

Low rising limb shape parameter occurs along the Great Plains, Mississippi Valley, Pacific coast, and the west of Gulf Coast (Fig. 5.c). In contrast, the shape parameter over the Rocky Mountains, High Plains, Great Basin, Pacific Northwest, and the Great Lakes region witnesses the highest values of rising limb shape parameters (Fig. 5.c). All the catchments located in the Southern states of the US (Cluster 9), Great Plains and North American deserts

(Cluster 8), and the Central Plains (Cluster 2) characterize low values of rising limb shape parameters (Fig. 6.c). This is due to low water availability, low snow fraction precipitation falling as snow, low leaf area index, and high evaporation experienced in these regions (Jehn et al., 2020). Excessive evaporation and a low snow fraction of precipitation falling as snow can contribute to low discharge and thus lower rising limb shape parameters. It is noted that the rising limb shape parameter indicates (Table 2) a positive correlation with vegetation attributes (r = 0.41 for forest fraction) and the fraction of precipitation falling as snow (r = 0.53), mean slope (r = 0.36), mean elevation (r = 0.41), and sand fraction (r = 0.37) whereas, it negatively correlates with precipitation frequency (r= -0.42 for high precipitation frequency and r = -0.45 for low precipitation frequency). High values of rising limb shape parameters are seen in Clusters 3, 4 (Fig. 6.c) located in the Northwestern Forested Mountains of the western US (Figure S2), dominant with a summer peak of discharge caused by rapid snowmelt. The rapid snowmelt can cause flashy hydrographs with high values of rising limb shape parameters.

Catchments with a high falling limb density are predominantly located along the Great Basin and the Rocky Mountains and in the High Plains region (Fig. 7.a). This is due to less forest cover in these arid regions and falling limb density shows a positive association with the arid climate (r = 0.39) (Table 2). Clusters 6, 7 (Fig. 8.a) over Marine West Coast Forests and Western Cordillera (Table S2) experience smaller falling limb densities. We can see that falling limb density is mainly governed by climate indices and is negatively correlated with the land cover characteristics (for LAI maximum (r = -0.37) and green veg frac max (r = -0.40), Table 2). Mean elevation (r = 0.55) also strongly characterizes the nature of the falling limb density (Table 2). Besides, fraction of precipitation falling as snow (r = 0.42) is also positively correlated with falling limb density (Table 2).

Similarities exist between the patterns of the upper recession coefficient and the lower recession coefficient (Fig. 7.b and Fig. 7.c). Clusters 3, 4 located in the Northwestern Forested Mountains (Figure S2), which have overall low discharge, show low values of upper and lower recession coefficients (Fig. 8.b and Fig. 8.c). Clusters 2 and 9, located in the eastern US, witness high values of recession coefficients; due to low slope inclinations (Jehn et al., 2020), water takes a long time to reach the outlet (Fig. 8.b and Fig. 8.c). Recession coefficients are negatively correlated (Table 2) with topographic indices (with mean elevation: $upper\_r = -0.40$, $lower\_r = -0.35$; with mean slope: $upper\_r = -0.38$, $lower\_r = -0.37$, where $upper\_r$ and $lower\_r$ corresponds to correlation values of upper and lower recession coefficients respectively). Further, the recession coefficients show a positive correlation with clay ($upper\_r = 0.52$, $lower\_r = 0.32$) and negative correlations with the fraction of precipitation falling as snow ($upper\_r = -0.46$, $lower\_r = -0.39$), forest fraction ($upper\_r = -0.31$, $lower\_r = -0.28$), and sand fraction ($upper\_r = -0.38$, $lower\_r = -0.23$, Table 2). Moreover, the geology attributes such as subsurface porosity ($upper\_r = 0.13$, $lower\_r = 0.16$) reveal a positive correlation to recession coefficients and a negative ($upper\_r = -0.09$, $lower\_r = -0.18$) with subsurface permeability (Table 2).

340
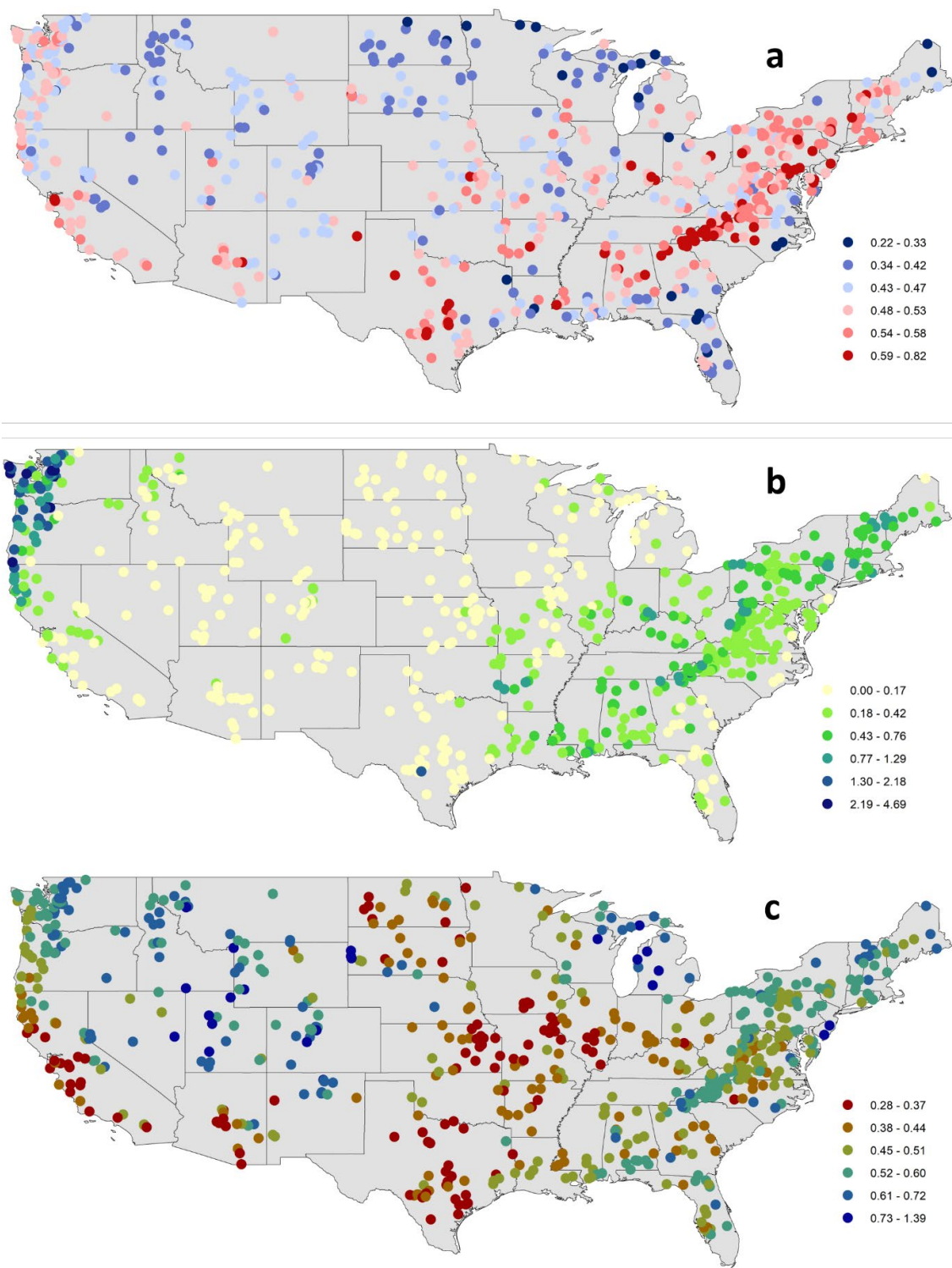
Figure 5. Spatial maps of streamflow indices associated with a rising limb (a) rising limb density [day^{-1}], (b)
rising limb scale parameter, (c) rising limb shape parameter over the CONUS**.**

343

344
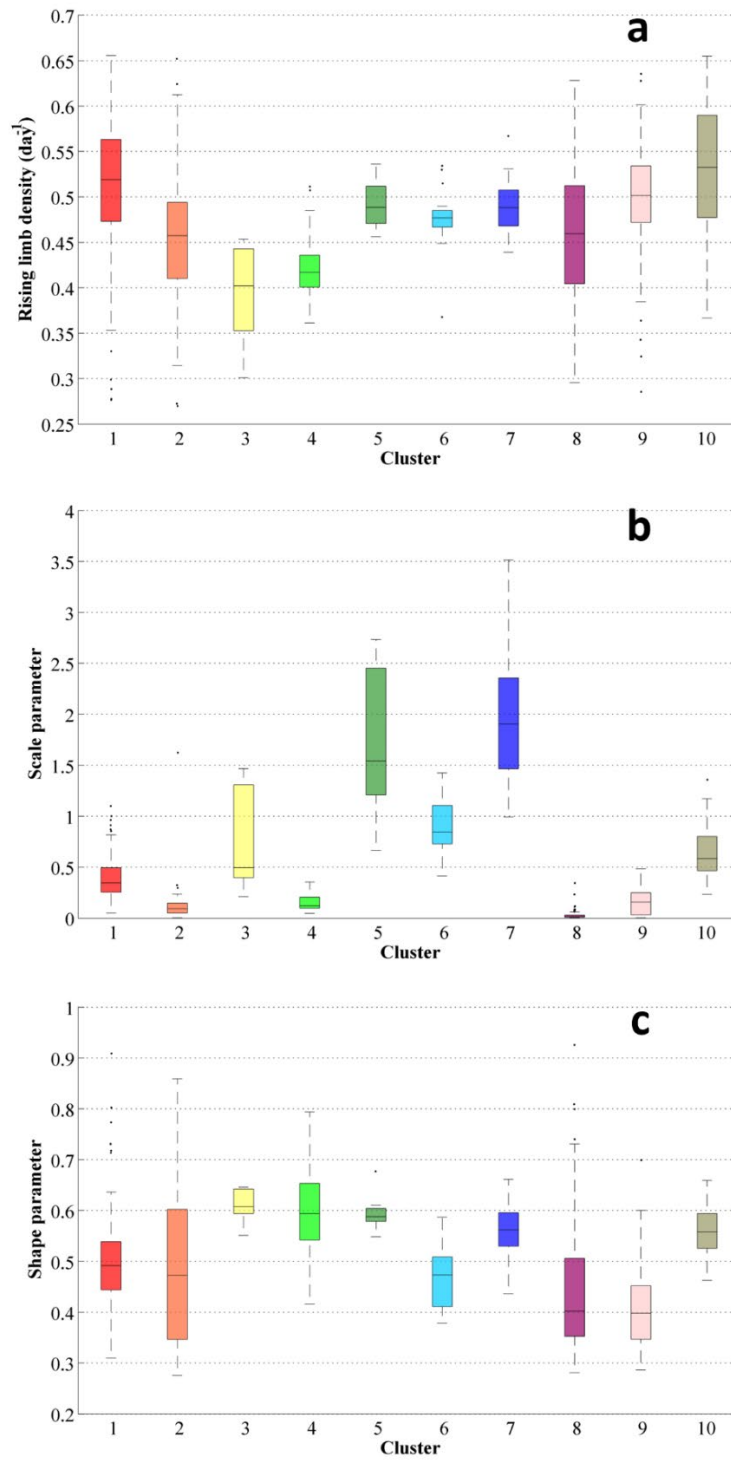
Figure 6. Boxplots of the hydrological descriptors linked with the rising limb (a) rising limb density [day^{-1}], (b) rising limb scale parameter, (c) rising limb shape parameter of the clusters over the CONUS.

347
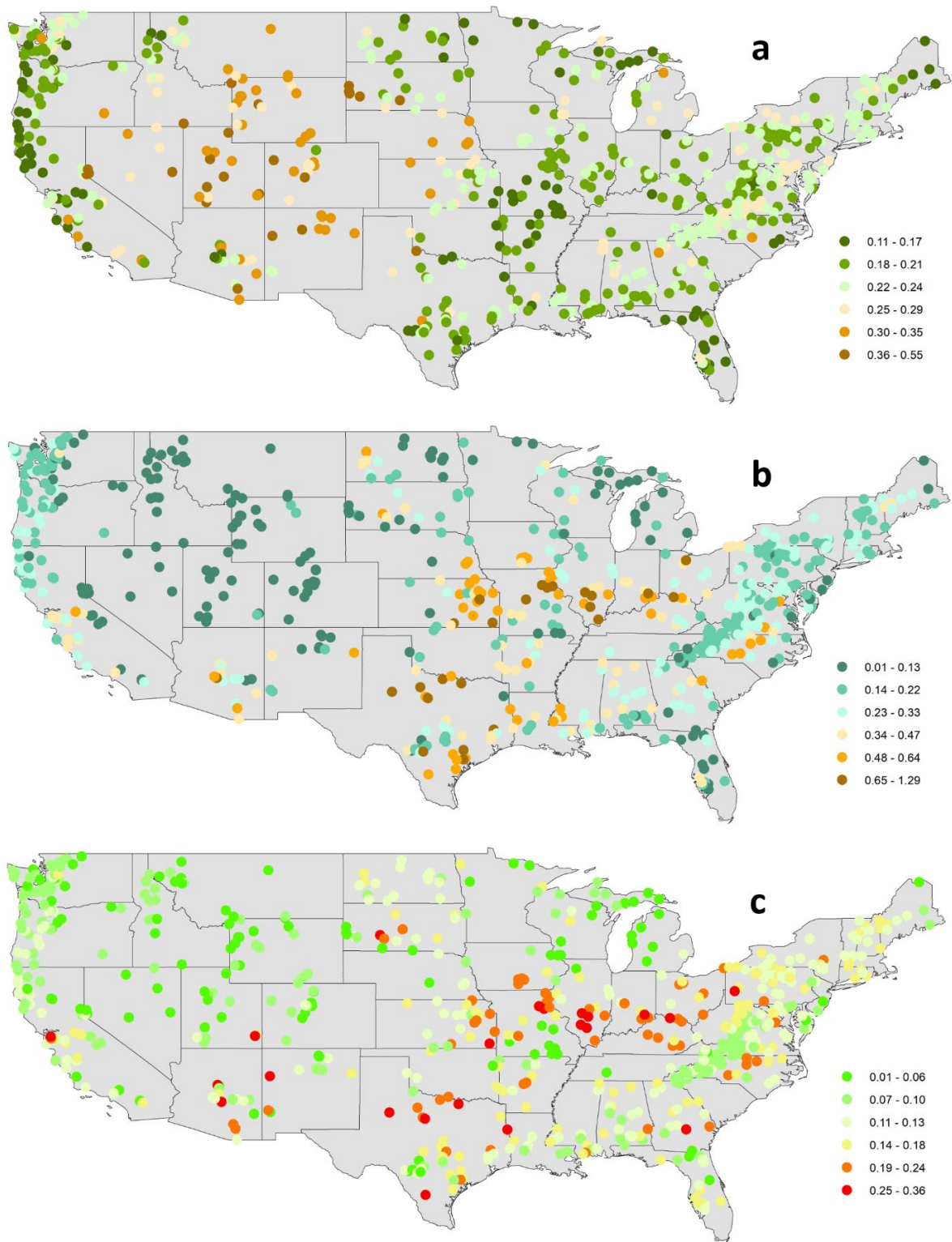
Figure 7. Regional variability of streamflow indices associated with the falling limb (a) falling limb density
[day^{-1}], (b) upper recession coefficient, (c) lower recession coefficient over the CONUS.

350
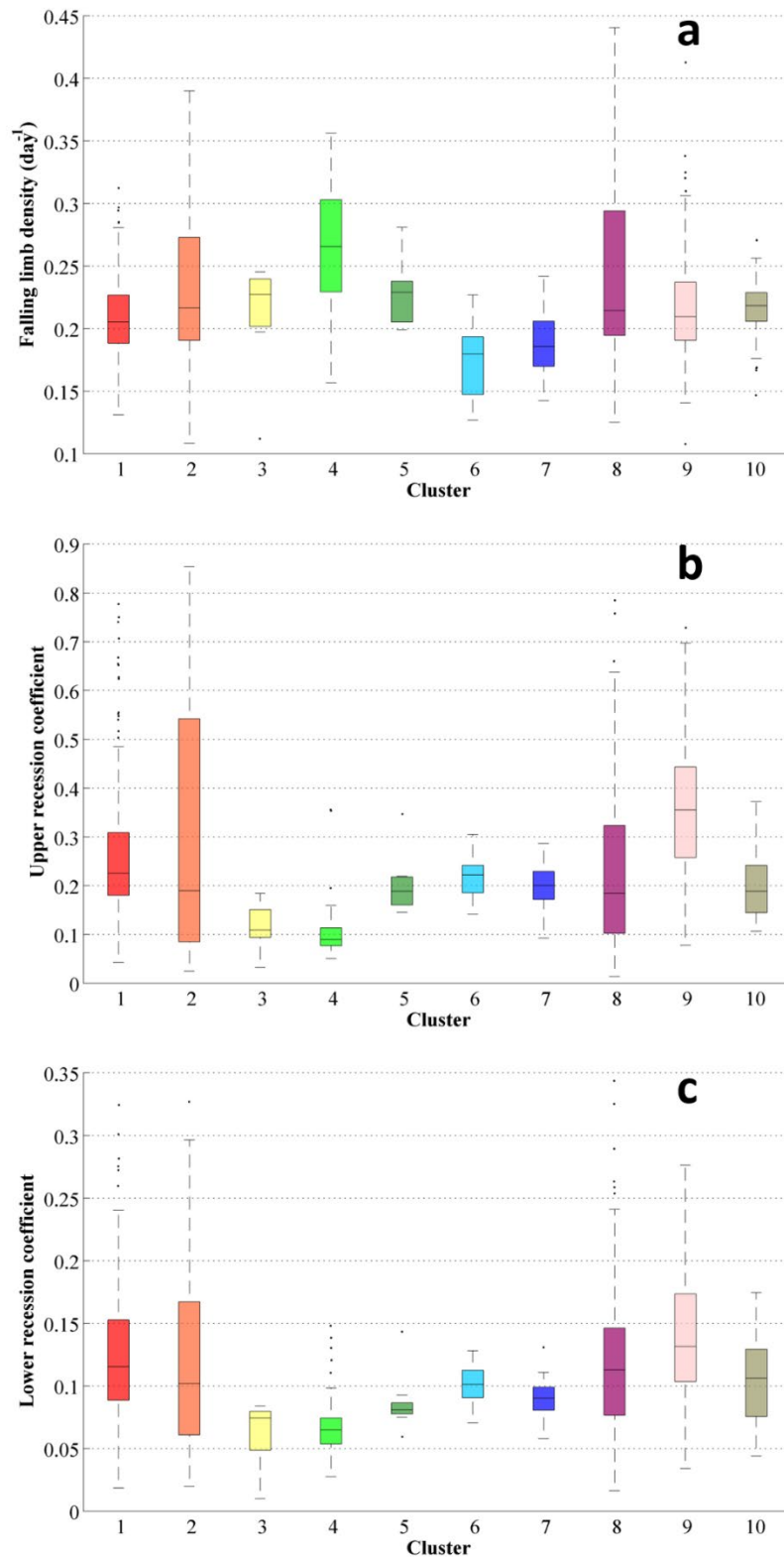
Figure 8. Boxplots of the streamflow indices related with the falling limb (a) falling limb density [day^{-1}], (b) upper recession coefficient, (c) lower recession coefficient of the clusters.

353

354

355 **Table 2** Correlation (r- values) between streamflow indices and the catchment attributes. Corresponding (*p*-
356 values) are shown in brackets. Insignificant correlations (*p* > 0.05) are marked in italics.

r- value	Rising limb density	Scale parameter	Shape parameter	Falling limb density	Upper recession coefficient	Lower recession coefficient
Area	-0.30 (0.00)	-0.17 (0.00)	*-0.06 (0.11)*	-0.13 (0.00)	*-0.06 (0.10)*	*-0.06 (0.11)*
Mean elevation	-0.20 (0.00)	-0.13 (0.00)	0.41 (0.00)	0.55 (0.00)	-0.40 (0.00)	-0.35 (0.00)
Mean slope	*-0.06 (0.13)*	0.35 (0.00)	0.36 (0.00)	0.18 (0.00)	-0.38 (0.00)	-0.37 (0.00)
Precipitation seasonality	*-0.04 (0.26)*	-0.36 (0.00)	-0.14 (0.00)	*0.01 (0.75)*	0.17 (0.00)	0.22 (0.00)
Frac of precp as snow	-0.33 (0.00)	*-0.04 (0.27)*	0.53 (0.00)	0.42 (0.00)	-0.46 (0.00)	-0.39 (0.00)
Aridity	-0.10 (0.01)	-0.53 (0.00)	-0.16 (0.00)	0.39 (0.00)	*0.04 (0.30)*	*0.03 (0.45)*
High precp freq	0.08 (0.04)	-0.56 (0.00)	-0.42 (0.00)	0.12 (0.00)	0.31 (0.00)	0.27 (0.00)
High precp dur	-0.15 (0.00)	*0.00 (0.97)*	*-0.07 (0.09)*	0.12 (0.00)	-0.11 (0.01)	-0.17 (0.00)
Low precp freq	*0.00 (0.91)*	-0.63 (0.00)	-0.45 (0.00)	0.17 (0.00)	0.26 (0.00)	0.19 (0.00)
Low precp dur	*-0.03 (0.49)*	-0.25 (0.00)	-0.29 (0.00)	0.11 (0.00)	*0.07 (0.07)*	*0.01 (0.84)*
Depth to bedrock	-0.32 (0.00)	-0.21 (0.00)	-0.16 (0.00)	-0.19 (0.00)	0.19 (0.00)	0.21 (0.00)
Sand frac	-0.28 (0.00)	*-0.02 (0.62)*	0.37 (0.00)	*-0.02 (0.63)*	-0.38 (0.00)	-0.23 (0.00)
Clay frac	0.26 (0.00)	-0.15 (0.00)	-0.47 (0.00)	*0.00 (0.93)*	0.52 (0.00)	0.32 (0.00)
Forest frac	0.10 (0.01)	0.46 (0.00)	0.41 (0.00)	-0.17 (0.00)	-0.31 (0.00)	-0.28 (0.00)
LAI maximum	0.20 (0.00)	0.41 (0.00)	0.17 (0.00)	-0.37 (0.00)	-0.09 (0.03)	*-0.04 (0.28)*
Green veg frac max	0.18 (0.00)	0.44 (0.00)	0.15 (0.00)	-0.40 (0.00)	*-0.05 (0.16)*	*-0.01 (0.74)*
Subsurface porosity	-0.16 (0.00)	*-0.06 (0.12)*	-0.16 (0.00)	-0.08 (0.03)	0.13 (0.00)	0.16 (0.00)
Subsurface permeability	-0.11 (0.00)	*-0.04 (0.34)*	*0.06 (0.12)*	*0.03 (0.39)*	-0.09 (0.02)	-0.18 (0.00)

357
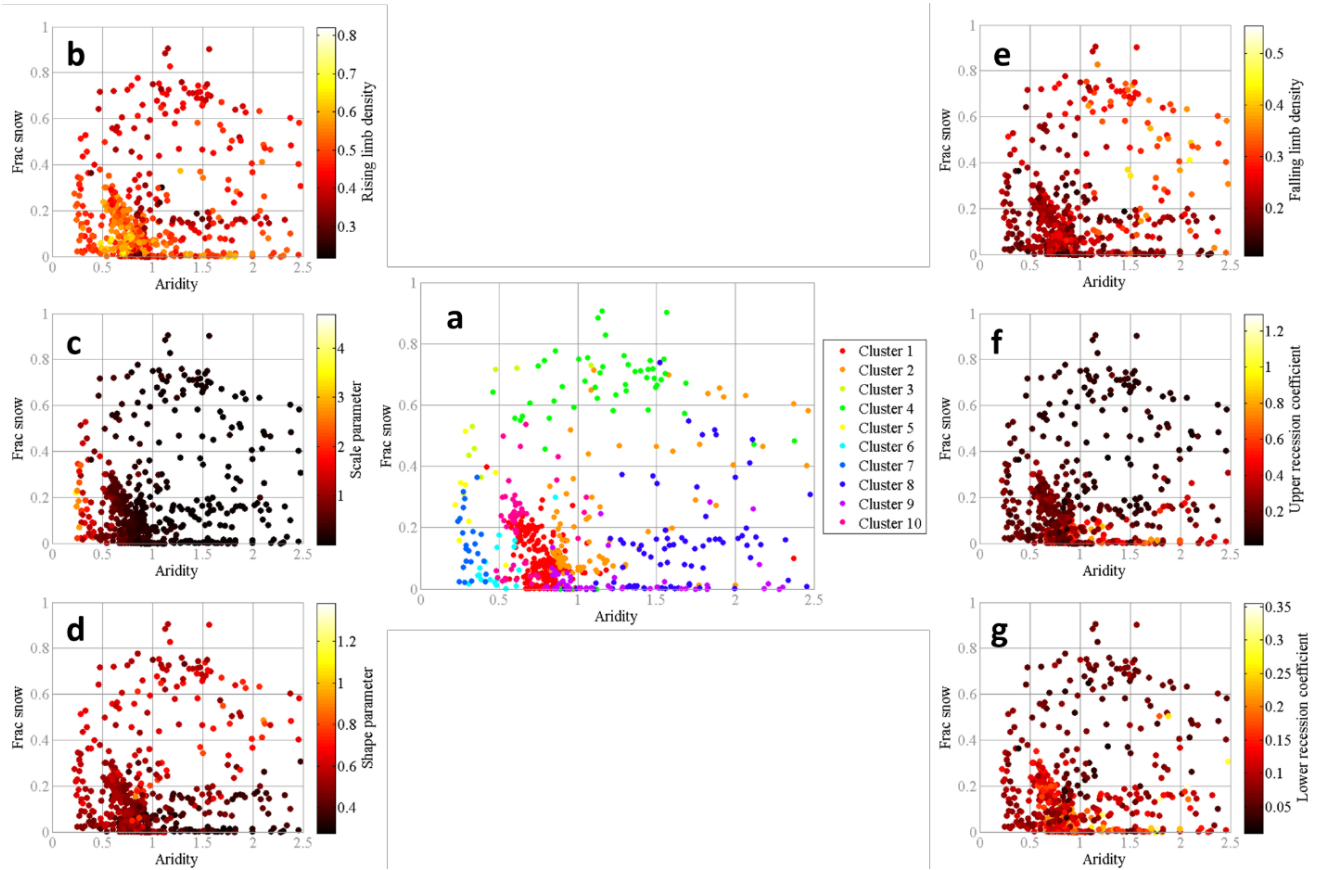
Figure 9. (a) Comparison of the hydrological clusters of Jehn et al. (2020) with the climate index space (fraction of precipitation falling as snow vs. aridity). Single dots show the catchments and are colored by their hydrological clusters. Comparison of the streamflow indices in climate index space (b) rising limb density (c) rising limb scale parameter, (d) rising limb shape parameter, (e) falling limb density, (f) upper recession coefficient, (g) lower recession coefficient for all catchments. Single dots show the catchments and are colored according to the value of the streamflow indices.

4.2 Influence of Attributes of Climate to Streamflow Indices

The climatic indices indicate a more substantial influence on hydrological signatures than the topographic, soil, land cover, and geological attributes combined (Addor et al., 2018, Stein et al., 2021). Additionally, the findings of Jehn et al. (2020) highlighted that the climate appears to be the most critical factor influencing hydrological behavior in the CAMELS dataset. Hence, the streamflow indices are examined in the climate index space (aridity along x-axis and fraction of precipitation falling as snow along the y-axis) to evaluate the main drivers of the catchments. Single dots show the catchments and are colored by their hydrological clusters (Fig. 9.a).

Clusters 5, 6, 7, 1, 10 are characterized by a low fraction of precipitation falling as snow and humid climate, whereas Clusters 3, 4 have humid climate experiencing a high fraction of precipitation falling as snow (Fig. 9.a). Clusters 2, 8, 9 are featured by a low fraction of precipitation falling as snow and arid climate (Fig. 9.a). The three categories mentioned above are referred to as G1, G2, and G3, respectively.

378 Clusters G1 with a low fraction of precipitation falling as snow with humid climate show (Clusters 1, 9, 10) high
379 rising limb densities (Fig. 9.b) and (Clusters 5, 7) high rising limb scale parameters (Fig. 9.c). This is because the
380 rising limb density negatively correlates with fraction of precipitation falling as snow (Table 2: r = -0.33, Fig.
381 9.b), whereas the rising limb scale parameter negatively correlates with aridity (Table 2: r = -0.53, Fig. 9.c).
382 Moreover, these Clusters G1 experience a low value of (Clusters 6, 7) falling limb density (Fig. 9.e). This is
383 because the falling limb density positively correlates with the climate indices (Table 2: r = 0.42 for fraction of
384 precipitation falling as snow and r = 0.39 for aridity, Fig. 9.e).

385 As mentioned earlier, Clusters G2 with humid climate and with a high fraction of precipitation falling as snow
386 (Clusters 3, 4) display low values of rising limb density as rising limb density correlates negatively with the
387 fraction of precipitation falling as snow (Table 2: r = -0.33, Fig. 9.b). G2 witnesses higher values of rising limb
388 shape parameter due to its negative correlation with aridity (r = -0.16) and positive correlation with the fraction
389 of precipitation falling as snow (Table 2: r = 0.53, Fig. 9.d). Furthermore, the Clusters of G2 (Clusters 3, 4) show
390 low values of recession coefficients as they depict a strong negative correlation with the fraction of precipitation
391 falling as snow (Table 2: upper_r = -0.46, and lower_r = -0.39, Fig. 9.f, g).

392 Low values of rising limb scale and shape parameters are noticed for the Clusters 2, 9, 8 (Clusters G3) with arid
393 climate and low fraction of precipitation falling as snow (Fig. 9.c, d) due to its negative correlation with aridity as
394 stated earlier. Cluster 8 experiences the maximum values of falling limb density (Fig. 9.e) where the region
395 witnesses low fraction of snow and arid catchments, due to its strong positive correlates with the aridity (r = 0.39,
396 Table 2).

5 Concluding remarks

398 Streamflow hydrograph portrays the time distribution of runoff at the point of measurement by a single curve, and
399 the hydrographs are characterized by their time irreversibility property. In this study, the indices related to this
400 characteristic feature are used to study the catchment drivers of streamflow hydrograph. The streamflow indices
401 associated with the time irreversibility of hydrograph open new opportunities to investigate the interaction
402 between topography, soil, climate, vegetation, geology that drive the hydrological behavior of catchments.
403 Moreover, most of the previously presented hydrologic indices are employed only for time-symmetric processes
404 (McMillan, 2021); the importance of the time irreversibility of streamflow is highlighted in this study. The indices
405 associated with rising and falling limbs are primarily correlated to distinct catchment attributes, establishing a
406 relationship between the indices and catchment attributes such as climate, topography, soil, geology, and
407 vegetation to delineate the controlling drivers in corresponding hydrograph sections. A set of streamflow indices
408 with temporal asymmetry for 671 catchments in the United States is presented in this study. The regional
409 variations among catchments over the United States are compared and discussed using the spatial maps of
410 streamflow indices. Such spatial maps of the streamflow indices supplement the hydrometeorological time series
411 and catchment attributes provided by Addor et al. (2017).

412 The study showed that the rising limb density is mainly governed by the elevation and fraction of precipitation
413 falling as snow. Climate indices, mean elevation, and the fraction of precipitation falling as snow mainly influence
414 falling limb density. In contrast, the aridity and frequency of precipitation drive the rising limb scale parameter.
415 Furthermore, forest fraction, the fraction of precipitation falling as snow, mean slope, mean elevation, sand

416 fraction, and precipitation frequency influence the rising limb shape parameter. Mean elevation, mean slope, clay,

417 the fraction of precipitation falling as snow, forest fraction, and sand fraction all determine recession coefficients.

418 Finally, streamflow indices are studied in the climate index space to isolate the runoff generation's leading drivers.

419 High rising limb densities and rising limb scale parameters are observed in catchments with low precipitation

420 falling as snow and a humid climate. It is observed that the catchments with a humid climate and a high fraction

421 of precipitation falling as snow display low values of rising limb density, high values of the rising limb shape

422 parameter, and low values of recession coefficients. The lowest values of rising limb scale and shape parameters,

423 and the highest values of falling limb density, are seen in catchments of arid climates and a low fraction of

424 precipitation falling as snow.

425 In general, the contribution of this work lies in differentiating hydrographs depending on their time irreversibility

426 property and using the corresponding indices to provide an alternative methodology for identifying the drivers of

427 streamflow hydrographs. In the context of large sample hydrology research, the concept of time-irreversibility

428 and the indices associated with it could also be used to describe the drivers at catchment scale. It must be noted

429 that each attribute (e.g., climate vegetation, soil, geology) usually does not exist alone in space but is closely

430 interwoven, resulting in strongly correlated attributes in a catchment (Jehn et al., 2020; Stein et al., 2021).

431 However, it would be beyond the scope of this paper to describe all probable relationships between attributes.

432 Keeping this in mind, the main focus of this study was constrained to only identify the controlling attributes of

433 streamflow indices. Another limitation of the work is related with the characterization of recessions used. Future

434 work may investigate using the inflection point or another recession separation technique to characterize

435 recessions.

436

437 *Data availability.* The CAMELS dataset can be found at https://doi.org/10.5194/hess21-5293-2017 (Addor et al.

438 2017). The hydrometeorological time series (https://doi.org/10.5065/D6MW2F4D) used in this paper are freely

439 available online.

440 *Competing interests.* The authors declare that they have no conflict of interest.

441 *Acknowledgements.* We would like to thank all the people who created the CAMELS dataset. We sincerely thank

442 Editor Elena Toth, Dr. Wouter Knoben, and the anonymous reviewer for patiently reviewing the manuscript and

443 offering valuable critical comments to improve the manuscript. Their suggestions have significantly improved the

444 quality of our contribution to this revised manuscript.

445 The funding received from the Ministry of Earth Sciences (MoES), Government of India, through the project,

446 "Advanced Research in Hydrology and Knowledge Dissemination", Project No.: MOES/PAMC/H&C/41/2013-

447 PC-II, is gratefully acknowledged.

448

449 **References**

450

451 Addor, Newman, A. J., Mizukami, N. and Clark, M. P.: The CAMELS data set: catchment attributes and

452 meteorology for large-sample studies, Hydrol. Earth Syst. Sci., 21(10), 5293–5313, doi:10.5194/hess-21-5293-

453 2017, 2017.

454 Addor, Nearing, G., Prieto, C., Newman, A. J., Le Vine, N. and Clark, M. P.: A Ranking of Hydrological
455 Signatures Based on Their Predictability in Space, Water Resour. Res., 54(11), 8792–8812,
456 doi:10.1029/2018WR022606, 2018.

457 Addor, N., Do, H. X., Alvarez-Garreton, C., Coxon, G., Fowler, K. and Mendoza, P. A.: Large-sample hydrology:
458 recent progress, guidelines for new datasets and grand challenges, Hydrol. Sci. J., 65(5), 712–725,
459 doi:10.1080/02626667.2019.1683182, 2020.

460 Alvarez-Garreton, C., Mendoza, P. A., Pablo Boisier, J., Addor, N., Galleguillos, M., Zambrano-Bigiarini, M.,
461 Lara, A., Puelma, C., Cortes, G., Garreaud, R., McPhee, J. and Ayala, A.: The CAMELS-CL dataset: Catchment
462 attributes and meteorology for large sample studies-Chile dataset, Hydrol. Earth Syst. Sci., 22(11), 5817–5846,
463 doi:10.5194/hess-22-5817-2018, 2018a.

464 Alvarez-Garreton, C., Mendoza, P. A., Boisier, J. P., Addor, N., Galleguillos, M., Zambrano-Bigiarini, M., Lara,
465 A., Puelma, C., Cortes, G., Garreaud, R., McPhee, J. and Ayala, A.: The CAMELS-CL dataset: catchment
466 attributes and meteorology for large sample studies – Chile dataset, Hydrol. Earth Syst. Sci., 22(11), 5817–5846,
467 doi:10.5194/hess-22-5817-2018, 2018b.

468 Arsenault, R., Bazile, R., Ouellet Dallaire, C. and Brissette, F.: CANOPEX: A Canadian hydrometeorological
469 watershed database, Hydrol. Process., 30(15), 2734–2736, doi:10.1002/hyp.10880, 2016.

470 Berghuijs, W. R., Sivapalan, M., Woods, R. A. and Savenije, H. H. G.: Patterns of similarity of seasonal water
471 balances: A window into streamflow variability over a range of time scales, Water Resour. Res., 50(7), 5638–
472 5661, doi:10.1002/2014WR015692, 2014.

473 Blöschl, G., Hall, J., Viglione, A., Perdigão, R. A. P., Parajka, J., Merz, B., Lun, D., Arheimer, B., Aronica, G.
474 T., Bilibashi, A., Boháč, M., Bonacci, O., Borga, M., Čanjevac, I., Castellarin, A., Chirico, G. B., Claps, P.,
475 Frolova, N., Ganora, D., Gorbachova, L., Gül, A., Hannaford, J., Harrigan, S., Kireeva, M., Kiss, A., Kjeldsen, T.
476 R., Kohnová, S., Koskela, J. J., Ledvinka, O., Macdonald, N., Mavrova-Guirguinova, M., Mediero, L., Merz, R.,
477 Molnar, P., Montanari, A., Murphy, C., Osuch, M., Ovcharuk, V., Radevski, I., Salinas, J. L., Sauquet, E., Šraj,
478 M., Szolgay, J., Volpi, E., Wilson, D., Zaimi, K. and Živković, N.: Changing climate both increases and decreases
479 European river floods, Nature, 573(7772), 108–111, doi:10.1038/s41586-019-1495-6, 2019.

480 Clark, M. P., McMillan, H. K., Collins, D. B. G., Kavetski, D. and Woods, R. A.: Hydrological field data from a
481 modeller's perspective: Part 2: Process-based evaluation of model hypotheses, Hydrol. Process., 25(4), 523–543,
482 doi:10.1002/hyp.7902, 2011.

483 Coxon, G., Freer, J., Wagener, T., Odoni, N. A. and Clark, M.: Diagnostic evaluation of multiple hypotheses of
484 hydrological behaviour in a limits-of-acceptability framework for 24 UK catchments, Hydrol. Process., 28(25),
485 6135–6150, doi:10.1002/hyp.10096, 2014.

486 Coxon, G., Addor, N., Bloomfield, J. P., Freer, J., Fry, M., Hannaford, J., Howden, N. J. K., Lane, R., Lewis, M.,
487 Robinson, E. L., Wagener, T. and Woods, R.: CAMELS-GB: hydrometeorological time series and landscape
488 attributes for 671 catchments in Great Britain, Earth Syst. Sci. Data, 12(4), 2459–2483, doi:10.5194/essd-12-
489 2459-2020, 2020.

490 Do, H. X., Gudmundsson, L., Leonard, M. and Westra, S.: The Global Streamflow Indices and Metadata Archive
491 (GSIM) – Part 1: The production of a daily streamflow archive and metadata, Earth Syst. Sci. Data, 10(2), 765–

785, doi:10.5194/essd-10-765-2018, 2018.

Duan, Q., Schaake, J., Andréassian, V., Franks, S., Goteti, G., Gupta, H. V., Gusev, Y. M., Habets, F., Hall, A., Hay, L., Hogue, T., Huang, M., Leavesley, G., Liang, X., Nasonova, O. N., Noilhan, J., Oudin, L., Sorooshian, S., Wagener, T. and Wood, E. F.: Model Parameter Estimation Experiment (MOPEX): An overview of science strategy and major results from the second and third workshops, J. Hydrol., 320(1–2), 3–17, doi:10.1016/j.jhydrol.2005.07.031, 2006.

Ehret, U., Gupta, H. V., Sivapalan, M., Weijs, S. V., Schymanski, S. J., Blöschl, G., Gelfan, A. N., Harman, C., Kleidon, A., Bogaard, T. A., Wang, D., Wagener, T., Scherer, U., Zehe, E., Bierkens, M. F. P., Di Baldassarre, G., Parajka, J., van Beek, L. P. H., van Griensven, A., Westhoff, M. C. and Winsemius, H. C.: Advancing catchment hydrology to deal with predictions under change, Hydrol. Earth Syst. Sci., 18(2), 649–671, doi:10.5194/hess-18-649-2014, 2014.

Ghiggi, G., Humphrey, V., Seneviratne, S. I. and Gudmundsson, L.: GRUN: an observation-based global gridded runoff dataset from 1902 to 2014, Earth Syst. Sci. Data, 11(4), 1655–1674, doi:10.5194/essd-11-1655-2019, 2019.

Gudmundsson, L., Do, H. X., Leonard, M. and Westra, S.: The Global Streamflow Indices and Metadata Archive (GSIM) – Part 2: Quality control, time-series indices and homogeneity assessment, Earth Syst. Sci. Data, 10(2), 787–804, doi:10.5194/essd-10-787-2018, 2018.

Gupta, H. V., Perrin, C., Blöschl, G., Montanari, A., Kumar, R., Clark, M. and Andréassian, V.: Large-sample hydrology: a need to balance depth with breadth, Hydrol. Earth Syst. Sci., 18(2), 463–477, doi:10.5194/hess-18-463-2014, 2014.

Jehn, F. U., Bestian, K., Breuer, L., Kraft, P. and Houska, T.: Using hydrological and climatic catchment clusters to explore drivers of catchment behavior, Hydrol. Earth Syst. Sci., 24(3), 1081–1100, doi:10.5194/hess-24-1081-2020, 2020.

Khrystyuk, B., Gorbachova, L. and Koshkina, O.: The impact of climatic conditions of spring flood formation on hydrograph shape of the Desna River, Meteorol. Hydrol. Water Manag., 5(1), 63–70, doi:10.26491/mhwm/67914, 2017.

Knoben, W. J. M., Woods, R. A. and Freer, J. E.: A Quantitative Hydrological Climate Classification Evaluated With Independent Streamflow Data, Water Resour. Res., 54(7), 5088–5109, doi:10.1029/2018WR022913, 2018.

Koutsoyiannis, D.: Simple stochastic simulation of time irreversible and reversible processes, Hydrol. Sci. J., doi:10.1080/02626667.2019.1705302, 2020.

Kuentz, A., Arheimer, B., Hundecha, Y. and Wagener, T.: Understanding hydrologic variability across Europe through catchment classification, Hydrol. Earth Syst. Sci., 21(6), 2863–2879, doi:10.5194/hess-21-2863-2017, 2017.

Linke, S., Lehner, B., Ouellet Dallaire, C., Ariwi, J., Grill, G., Anand, M., Beames, P., Burchard-Levine, V., Maxwell, S., Moidu, H., Tan, F. and Thieme, M.: Global hydro-environmental sub-basin and river reach characteristics at high spatial resolution, Sci. Data, 6(1), 283, doi:10.1038/s41597-019-0300-6, 2019.

Mathai and Mujumdar, P. P.: Multisite Daily Streamflow Simulation With Time Irreversibility, Water Resour.

Res., 55(11), 9334–9350, doi:10.1029/2019WR025058, 2019.

McMillan, H. K.: A review of hydrologic signatures and their applications, WIREs Water, 8(1), 1–23, doi:10.1002/wat2.1499, 2021.

McMillan, H. K., Clark, M. P., Bowden, W. B., Duncan, M. and Woods, R. A.: Hydrological field data from a modeller's perspective: Part 1. Diagnostic tests for model structure, Hydrol. Process., 25(4), 511–522, doi:10.1002/hyp.7841, 2011.

Newman, A. J., Clark, M. P., Sampson, K., Wood, A., Hay, L. E., Bock, A., Viger, R. J., Blodgett, D., Brekke, L., Arnold, J. R., Hopson, T. and Duan, Q.: Development of a large-sample watershed-scale hydrometeorological data set for the contiguous USA: data set characteristics and assessment of regional variability in hydrologic model performance, Hydrol. Earth Syst. Sci., 19(1), 209–223, doi:10.5194/hess-19-209-2015, 2015.

Richter, B. D., Baumgartner, J. V., Powell, J. and Braun, D. P.: A Method for Assessing Hydrologic Alteration within Ecosystems, Conserv. Biol., 10(4), 1163–1174, doi:10.1046/j.1523-1739.1996.10041163.x, 1996.

Roberts, M. C. and Klingeman, P. C.: The influence of landform and precipitation parameters on flood hydrographs, J. Hydrol., 11(4), 393–411, doi:10.1016/0022-1694(70)90004-1, 1970.

Rogers, W. F.: New concept in hydrograph analysis, Water Resour. Res., 8(4), 973–981, doi:10.1029/WR008i004p00973, 1972.

Sawicz, K., Wagener, T., Sivapalan, M., Troch, P. A. and Carrillo, G.: Catchment classification : empirical analysis of hydrologic similarity based on catchment function in the eastern USA, Hydrol. Earth Syst. Sci., 8(3), 2895–2911, doi:10.5194/hess-15-2895-2011, 2011.

Sawicz, K. A., Kelleher, C., Wagener, T., Troch, P., Sivapalan, M. and Carrillo, G.: Characterizing hydrologic change through catchment classification, Hydrol. Earth Syst. Sci., 18(1), 273–285, doi:10.5194/hess-18-273-2014, 2014.

Serinaldi, F. and Kilsby, C. G.: Irreversibility and complex network behavior of stream flow fluctuations, Phys. A Stat. Mech. its Appl., 450, 585–600, doi:10.1016/j.physa.2016.01.043, 2016.

Shamir, E., Imam, B., Morin, E., Gupta, H. V. and Sorooshian, S.: The role of hydrograph indices in parameter estimation of rainfall-runoff models, Hydrol. Process., 19(11), 2187–2207, doi:10.1002/hyp.5676, 2005.

Singh, V. P.: Effect of spatial and temporal variability in rainfall and watershed characteristics on stream flow hydrograph, Hydrol. Process., 11(12), 1649–1669, doi:10.1002/(SICI)1099-1085(19971015)11:12<1649::AID-HYP495>3.0.CO;2-1, 1997.

Stagge, J. H. and Moglen, G. E.: A nonparametric stochastic method for generating daily climate-adjusted streamflows, Water Resour. Res., 49, 6179–6193, doi:10.1002/wrcr.20448, 2013.

Stein, L., Clark, M. P., Knoben, W. J. M., Pianosi, F. and Woods, R. A.: How Do Climate and Catchment Attributes Influence Flood Generating Processes? A Large-Sample Study for 671 Catchments Across the Contiguous USA, Water Resour. Res., 57(4), 1–21, doi:10.1029/2020WR028300, 2021.

Szilagyi, J., Balint, G. and Csik, A.: Hybrid, Markov chain-based model for daily streamflow generation at multiple catchment sites, J. Hydrol. Eng., 11(3), 245–256, 2006.